Defect-Dependent Corrugation in Graphene

Fabian L. Thiemann,[1,2,3,4] Patrick Rowe,[1,2,3] Andrea Zen,[5,6,2] Erich A. Müller,[4] and Angelos Michaelides[3,1,2,a)]

[1)] *Department of Physics and Astronomy, University College London, Gower Street, London, WC1E 6BT, United Kingdom*

[2)] *Thomas Young Centre and London Centre for Nanotechnology, 17-19 Gordon Street, London WC1H 0AH, United Kingdom*

[3)] *Yusuf Hamied Department of Chemistry, University of Cambridge, Lensfield Road, Cambridge, CB2 1EW, United Kingdom*

[4)] *Department of Chemical Engineering, Imperial College London, South Kensington Campus, London SW7 2AZ, United Kingdom*

[5)] *Dipartimento di Fisica Ettore Pancini, Università di Napoli Federico II, Monte S. Angelo, I-80126 Napoli, Italy*

[6)] *Department of Earth Sciences, University College London, Gower Street, London WC1E 6BT, United Kingdom*

(Dated: This manuscript was compiled on 13 September 2021)

Graphene's intrinsically corrugated and wrinkled topology fundamentally influences its electronic, mechanical, and chemical properties. Experimental techniques allow the manipulation of pristine graphene and the controlled production of defects which allows to control the atomic out-of-plane fluctuations and, thus, tune graphene's properties. Here, we perform large scale machine learning-driven molecular dynamics simulations to understand the impact of defects on the structure of graphene. We find that defects cause significantly higher corrugation leading to a strongly wrinkled surface. The magnitude of this structural transformation strongly depends on the defect concentration and specific type of defect. Analysing the atomic neighborhood of the defects reveals that the extent of these morphological changes depends on the preferred geometrical orientation and the interactions between defects. While our work highlights that defects can strongly affect graphene's morphology, it also emphasises the differences between distinct types by linking the global structure to the local environment of the defects.

Keywords: graphene, defects, nanoengineering

Graphene's remarkable properties strongly depend on its morphology with many physical phenomena arising as a consequence of its intrinsic ripples[1] and corrugation[2–10] or by the presence of defects.[11–25] For instance, introducing eight-membered-ring defects can enhance graphene's ion permeability.[26–28] This makes graphene an ideal candidate for nanoengineering where material properties are tuned by modifying the atomic morphology.[29,30] To this end, a plethora of experimental techniques has emerged ranging from the atomically precise insertion of defects via electron beam[30–38] or ion bombardment[31,39–42] to chemical etching with KOH[43,44] and the regulation of rippling patterns by inducing strain.[45] More recent approaches like laser-assisted chemical vapour deposition[46] or high temperature quenching[47] go one step further by incorporating the desired morphology *a priori* in the growth process.

The diversity of methods available to manipulate graphene's atomic structure highlights the potential of morphologically-modified graphene which is also reflected by the variety of exciting applications. In particular, our interest has been piqued by reports on the tuned capability of graphene in the fields of hydrogen storage,[48,49] catalysis,[50] and ultrahigh and fast adsorption of organic pollutants.[44,51] Introducing defects can significantly increase graphene's number of active sites due to both the reactive character of the defects itself[21,44,50] and the induced conformational transformation to a highly corrugated surface where wrinkles possess a high chemical activity.[6,52,53] The rippled and curled shape, moreover, ensures that the created active sites are accessible for adsorbates or chemical dopants[50] by expanding the surface area and preventing graphene sheets from stacking together.[44,49] It was also suggested, that the adsorption affinity of molecules is directly linked to the corrugation profile[44,53,54] indicating the opportunity for the selective removal of organic pollutants.

The impact of defects on graphene's structure is at the very heart of the applications described above raising the question of distinct deformation mechanisms. It is well known that even small deviations from a pristine hexagonal lattice, such as isolated pentagons or heptagons, can lead to a corrugated surface.[55–60] These induced morphological changes have been investigated for a variety of defects in graphene including dislocations (pentagon-heptagon dipoles),[61–63] vacancies,[64,65] topological defects,[66,67] adatoms,[68] and grain boundaries.[69–71] Several of these experimental[62,72] and computational[63,65,66,69] studies report a long-ranging interaction between defects which manifests itself in an out-of-plane buckling of the surface. These deformations are dictated by the type and arrangement

[a)] Electronic mail: am452@cam.ac.uk

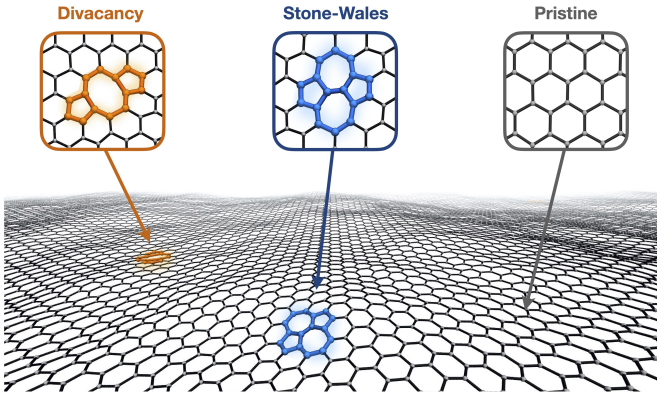

FIG. 1. Schematic illustration of graphene and the different defect types investigated in this letter and expected morphology in the limit of low defect concentrations. The atoms forming the defect are highlighted in orange and blue for divacancy and Stone-Wales defects, respectively.

of defects which has lead to fascinating work aiming to predict the unique arrangement of defects required to obtain a desired three-dimensional structure.[73–75] Notwithstanding the value of these studies, fundamental questions such as whether the magnitude of the induced corrugation varies between distinct types of defects or how the morphology changes for a highly defective system have yet to be systematically addressed. In fact, exploring the dependence of graphene's surface roughness on both the nature and number of defects present and revealing the specific mechanisms responsible for the structural transformation are of both theoretical and practical interest. In particular, it may contribute to a better understanding of the puzzling experiments reporting an enhancement of graphene's stiffness[76] and a vanishing thermal expansion coefficient[77] with an increasing vacancy concentration. Knowing the impact of defects on graphene's morphology *a priori*, would be a powerful tool to further tailor graphene's properties and, thus, accelerate the design and manufacture of graphene-based nanomaterials.

In this work, we investigate graphene's structural response to two common point defects,[22,78,79] namely divacancies and Stone-Wales[80] defects both visualised in figure 1. Stone-Wales defects represent the simplest example of a topological defect where a C-C bond rotation transforms four hexagons into two pentagons and heptagons. Conversely, divacancies are formed by the loss of two adjacent carbon atoms. Graphene's sp^2 network remains intact, however, by undergoing a reconstruction and the formation of one 8-membered and two 5-membered rings.[34,81] It is worth noting, however, that additional bond rotations can further transform the divacancy into more complex geometries comprising a rich variety of geometrical shapes including pentagons, hexagons, and heptagons[32] (see also supporting information).

We employ molecular dynamics (MD) simulations to explore the defect-induced alteration of graphene's structure. As the spatial extension of graphene's ripples[1,82] and long-range nature of the defect-defect interactions[62,65,66,72] make simulation studies with *ab initio* methods prohibitively expensive, classical force fields such as the long-range carbon order potential (LCBOP),[83] the reactive empirical bond order (REBO II) potential,[84] or the environment dependent interatomic potential (EDIP),[85] represent a computationally efficient alternative. In this work, however, we use the recently developed machine learning-based Gaussian approximation potential for carbon (GAP-20)[86] which has been carefully validated against experimental measurements and quantum mechanical calculations. Being trained on a database of *ab initio* structures comprising configurations ranging from pristine graphene to amorphous carbon, GAP-20 reliably describes the phonon spectrum of graphene as well as the defects' energetic and structural characteristics. By using GAP-20, our work represents the first systematic investigation of the interplay between defects and graphene's morphology based on large scale simulations approaching quantum mechanical accuracy. For a detailed description of GAP-20 including the selection of training data, chosen hyperparameters as well as a comprehensive benchmarking and comparison to other classical force fields the reader is referred to the original reference[86] while an extensive derivation of the theory behind the GAP framework can be found elsewhere..[87,88] In addition, in the supporting information we show that the GAP-20 accurately reproduces its *ab initio* reference for highly defective and corrugated graphene.

For both defect types, we perform simulations at room temperature for a varying concentrations ranging from $\approx 0.03\%$ for an isolated defect to 3% representing a highly defective system where the distance between defects reduces to ≈ 1 nm.

As the equilibrium concentration of the defects studied is negligible at room temperature due to their high formation energies,[22,79] the high concentrations investigated here can be in principle achieved by intentionally introducing defects through a variety of experimental methods described above. While divacancies are easily created, the controlled preparation of graphene samples comprising a large number of Stone-Wales defects remains experimentally challenging due to their short lifetime under electron beam irradiation.[32,33,89] From a theoretical point of view, however, Stone-Wales defects, being the fundamental example of topological disorder, represent a suitable reference to gain valuable insight into the type-dependent impact of defects on graphene's corrugation. Further, both Stone-Wales defects and divacancies do not, in contrast to adatoms,[90] migrate at room temperature preventing the coalescence or annihilation of defects and, thus, make the comparison

between the two types straightforward.

We find that the defective systems indeed exhibit a highly crumpled surface, the dimensions of which significantly exceed the expected out-of-plane deviations in pristine graphene, particularly at defect concentrations $> 0.5\%$. On a quantitative level, however, the impact of Stone-Wales and divacancy defects differs considerably with the latter leading to roughly two times higher corrugation at the same defect concentration. In order to understand this striking result, we examine the local environments of the defects introduced. Our analysis reveals that the magnitude of the distinct morphological change is an inherent feature of the defect which is determined by its geometry and the extent of defect-defect coupling.

The MD simulations were performed in LAMMPS[91] at a temperature of 300 K and zero stress on free-standing graphene sheets comprising between 6984 and 7200 carbon atoms equivalent to the system size used in our previous work.[82] The precise number of atoms depends on the number of defects. In analogy to previous work,[17] we define the defect concentration as the ratio of removed (2 per divacancy) or rotated (2 per Stone-Wales defect) atoms to the total number of atoms in a pristine graphene sheet. The defects were randomly distributed on the graphene sheet while satisfying a minimum distance criterion of 10 Å between defect centers. Each simulation was started from a perfectly flat surface and any reconstruction of vacancy defects happened naturally in the simulation and was not enforced by the initial configuration. To account for the impact of varying orientation and distance between defects, three simulations with different initial defect distributions were conducted for each type and concentration. All systems were equilibrated for 20 ps before statistics were collected for 150 ps for the defective systems. As pristine graphene serves as a reference system in our study, it is simulated for 1 ns to ensure a small statistical uncertainty and prevent error propagation when properties of defective systems are related to the pristine case. In the supporting information, we show that the properties investigated in this work can be obtained with these simulation times showing an error below 10 % with respect to tenfold longer trajectories. The entire post-processing analysis was done in Python using features from the ASE,[92] MDAnalysis,[93,94] and OVITO[95] software packages.

We start our investigation by analysing the structure of a graphene sheet in the absence and presence of defects. Here, we use the standard deviation of the atomic heights distribution sampled over all atoms and frames as a representative measure to quantify the morphology of the different systems. Rather than reporting absolute values, however, we express the height fluctuations of any system relative to those observed for pristine graphene and denote this ratio as the corrugation amplification factor (CAF, see also supporting information). While the atomic out-of-plane displacements intrinsically scale with the system's dimensions,[96–98] the CAF represents an intuitive and invariant property to assess whether certain defects have an enhancing or diminishing impact on graphene's corrugation.

In figure 2, we show the CAF as a function of the defect concentration for the two distinct types of structural defects. The CAF values differ significantly across the individual defect types and concentrations, ranging from approximately 1 (no morphological alteration with respect to pristine graphene) to 5 (substantial topological change). While the different simulations at equal concentrations of the same type yield remarkably similar results, it is noteworthy that scattering beyond the range of statistical errors of the measured CAFs is inevitable due to different initial defect distributions, particularly at high concentrations. The exact orientation and arrangement of defects can fundamentally affect graphene's properties[18,73] and also have been shown to determine which buckling modes are induced.[62]

Graphene comprising Stone-Wales defects or divacancies shows CAF values well above 1 even at relatively low concentrations of $\approx 0.2\%$, demonstrating their capability to increase the amplitude of the atomic height fluctuations. For both defect types, we initially observe a strong increase of the CAF before reaching a plateau at high concentrations $> 1.5\%$. At 3%, the highest concentration investigated, graphene's morphology differs fundamentally from the pristine condition by possessing an almost three-times and five-times more corrugated surface for Stone-Wales defects and divacancies, respectively. This strong dependence on the defect type and concentration is also reflected by the discrepancy of CAF values observed for differently reconstructed divacancies (see supporting information) indicating a high sensitivity of graphene's morphology with respect to small perturbations such as individual bond rotations. To visualise the dimension of the extreme structural transformations, snapshots from the simulations at a concentration of 1% are shown for both defect types and compared to pristine graphene on the right panel of figure 2. The defective graphene sheets show significant out-of-plane buckling differing fundamentally from the pristine system. Interestingly, the magnitude of this defect-induced corrugation is very similar to that of pristine graphene under compressive strain showing a CAF of ≈ 6 at a strain rate of -2% (see supporting information and references[82,99]).

The distinct trends observed in graphene's structural behaviour call for a detailed analysis of the atomic structure in the defects' vicinity to further understand the origin and mechanisms of the morphological transformations. To this end, we compute the average

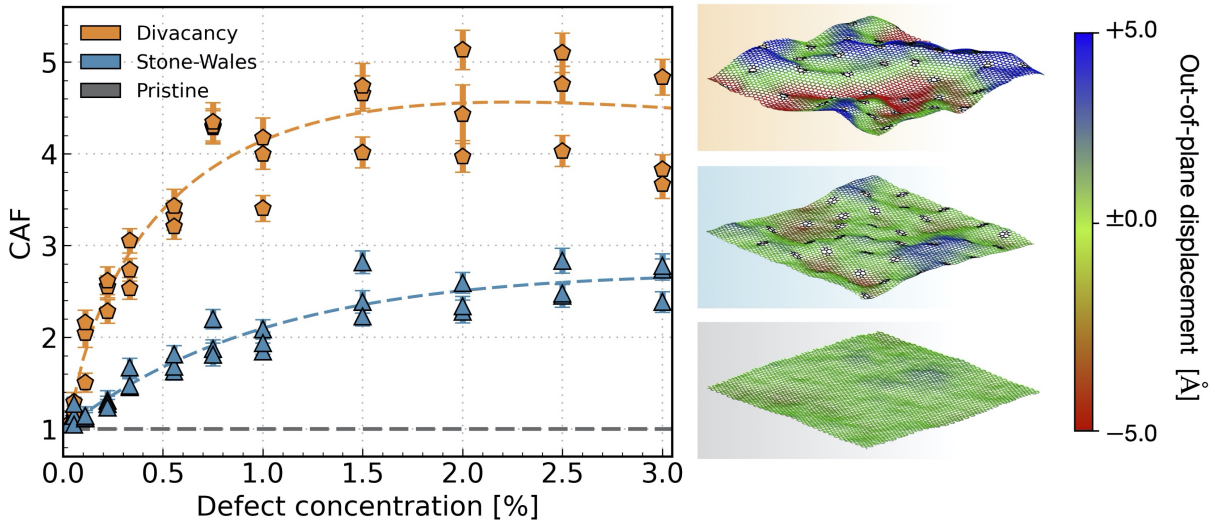

FIG. 2. Morphological transformation of graphene in the presence of different types of defects. The left panel depicts the dependence of the CAF on defect type and concentration. The CAF is a ratio of the corrugation of each defective system to pristine graphene and the values reported correspond to the simulation averages over all atoms and frames. The error bars represent the related statistical error obtained via block averaging. The dashed lines are intended as guides to the eye. On the right hand side, we show snapshots from the trajectories at 1% concentration for the two types of defect and for pristine graphene. The atoms are coloured according to their out-of-plane position relative to the center of mass of the graphene sheet and the defective atoms are highlighted in black.

inclination and Gaussian curvature of the defects' local environments as shown in the left panel of figure 3. Here, we describe these geometrical quantities based on an analytical height function $f_h(x, y)$ which is individually fitted to the atomic positions defining the local environment of each defect in the system. Having ensured an accurate description of the atomic landscape, first and second order spatial derivatives of $f_h(x, y)$ are computed along previously defined characteristic directions resembling the defect type's unique symmetry. The inclination and Gaussian curvature are then computed as the norm of the gradient and the determinant of the Hessian at the defect center, respectively.

To provide a baseline and get a grasp of the expected magnitudes, we evaluate both parameters on pristine graphene where three adjacent hexagons are employed as a defect proxy , as illustrated in the lower right panel of figure 3. As anticipated, local environments exclusively comprising hexagons show zero Gaussian curvature and the presence of wrinkles and ripples in pristine graphene can be attributed entirely to local tilting which we quantify here to be ≈ 0.066. Note that this non-zero inclination by no means contradicts the general requirement imposed by periodic boundary conditions of a flat surface on average where negative and positive atomic out-of-plane displacements balance each other out. Rather, it originates from strictly positive values of the geometric measure being based on the norm of the local height gradients and its magnitude is related to the overall surface roughness and corrugation.

While Stone-Wales defects show zero local Gaussian curvature, they exhibit a roughly four to five times larger tilt than unperturbed hexagons in pristine graphene. The high value of ≈ 0.270 for the isolated defect highlights that the strong inclination is an intrinsic feature of the Stone-Wales defect. It was shown by *ab initio* calculations[100] that it is energetically most favourable for the atoms forming the pentagons to move in opposite directions imposing a sine-like wave centered at the defect core. We observe the same trend for concentrations < 0.25 % where the total inclination can be almost exclusively attributed to the height gradient along the pentagon axis (see supporting information) as visualised in the center right panel of figure 3. A high defect concentration has a positive but rather small effect on the local inclination showing a maximum increase of $< 20\%$ reaching a plateau for concentrations > 1.5 %.

With an inclination and Gaussian curvature ranging from ≈ 0.086 to ≈ 0.33 and from ≈ -0.001 to ≈ -0.012, respectively, divacancies show a concentration dependence for both geometrical parameters. Based on the definition of the Gaussian curvature, negative values correspond to bending in opposing directions along orthogonal axes corresponding to a pringle[57] shape (hyperbolic paraboloid) as illustrated in figure 3. This curved shape is characteristic for divacancies and agrees well with the minimum energy configurations found with a classical potential[101] and density functional theory.[65]

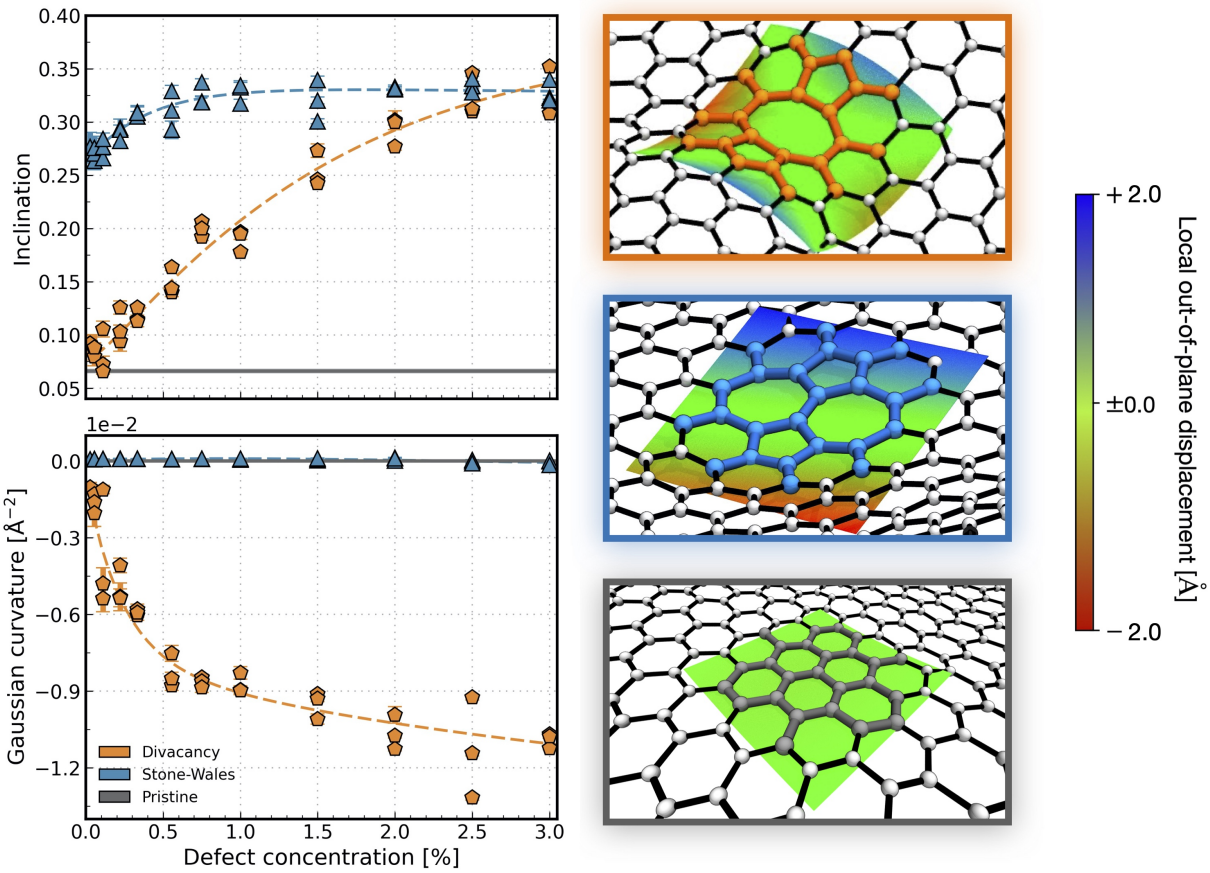

FIG. 3. Analysis of the geometrical properties of the defects' local environments. The left half of the figures shows the results for the local inclination (top) and Gaussian curvature (bottom) for all defect types as a function of concentration. For each property, the reported values correspond to averages over all defects and frames and the error bars represent the related statistical error obtained via block averaging. The solid lines correspond to the reference value obtained for pristine graphene and the dashed lines are intended as guides to the eye. On the right side, we show close-ups of simulation snapshots depicting the different systems: divacancies (orange), Stone-Wales defects (blue), and pristine graphene (grey). In each snapshot the atoms of the local environment of a defect are highlighted by thicker bonds and the colour of the respective defect type. The coloured surfaces correspond to the fitted function $f_h(x, y)$ for the respective defect which are coloured according to their local height relative to the center of mass of the defective atoms.

In contrast to Stone-Wales defects, however, we find a significant enhancement of both geometrical parameters by increasing the concentration leading to a roughly four and tenfold higher inclination and curvature, respectively, indicating strong defect-defect coupling.

Our analysis of the local environments reveals the origin behind the distinct morphological alterations for both defect types. The defects act as *corrugation seeds* and impose a distinct shift in the height distributions of the adjacent atoms to comply with the induced tilt and curvature, respectively. For dilute and very low concentrations, this phenomenon is mainly of local nature showing a decaying effect with increasing distance from the defect center resulting in a global morphology similar to that of pristine graphene. In the abundance of defects, conversely, the perturbations induced by individual *seeds* will superimpose and interfere with each other preventing the overall atomic height distribution from approaching the pristine limit. This effect can be enhanced if the defects strongly interact with each other as is shown in the case of divacancies.

Finally, as this is the first simulation study scanning the morphological impact of different point defects at varying concentrations and room temperature, a direct comparison to previous work is difficult. While a complete benchmarking of other potentials is beyond the scope of this work, we analysed trajectories obtained from MD simulations performed at defect concentration of 1 % based on the commonly employed LCBOP and REBO II force fields. Overall, the CAFs obtained with these potentials agree qualitatively with our findings. However, we note that both force fields overestimate the energy barrier associated with the reconstruction of the divacancy, requiring the simulation to be initialised with

reconstructed defects to obtain a corrugated morphology (see supporting information). Thus, simply using these potentials without prior knowledge of the influence defects have on the corrugation is unlikely to have revealed the insights obtained here.

In conclusion, we have reported a machine learning-based molecular dynamics study investigating the impact of Stone-Wales and divacancy defects at varying concentrations and room temperature on the morphological behaviour of graphene. In accordance with theory and chemical intuition, we find that defects can significantly enhance the system's corrugation even at low concentrations with the magnitude of the influence depending considerably on the nature of the defect. To further understand the mechanisms behind these trends, we compared the defects' local structure revealing an intrinsic tilt and curvature for Stone-Wales and divacancy defects, respectively, whereby the latter is strongly enhanced by defect-defect coupling. Our results underline the strong interplay between defects and graphene's corrugation indicating that the surprising mechanical properties[76,77] of defective graphene might be related to the substantially more wrinkled surface. Looking forward, in this work we exclusively focused on the structural alteration of free-standing graphene in the presence of defects of the same type. However, it will be relevant to investigate the coupling between different types of defects as well as the impact of substrate-induced strain on graphene's corrugation in future work. Likewise, it will be interesting to explore the impact of defects on the dynamics of the graphene ripples which have been shown to couple and dominate the motion of a water droplet on strained graphene.[102] By linking the global morphology in graphene to the fundamental nature of each defect type, our work represents a starting point to answering these questions and paves the way for precise nano-engineering of graphene in various applications ranging from the removal of organic pollutants[44,51] to lithium ion batteries.[103]

ACKNOWLEDGEMENTS

We thank Christoph Schran, Matthias Kiesel, Stephen J Cox, and Venkat Kapil for fruitful discussions throughout the course of this work. We are grateful to the UK Materials and Molecular Modelling Hub for computational resources, which is partially funded by EPSRC (EP/P020194/1 and EP/T022213/1). This work used the ARCHER UK National Supercomputing Service (http://www.archer.ac.uk) through our membership of the UK's HEC Materials Chemistry Consortium, which is funded by EPSRC (EP/L000202, EP/ R029431). We are also grateful for the computational resources granted by the UCL Grace High Performance Computing Facility (Grace@UCL), and associated support services. Calculations were also performed on the Cambridge Service for Data Driven Discovery (CSD3) operated by the University of Cambridge Research Computing Service (www.csd3.cam.ac.uk), provided by Dell EMC and Intel using Tier-2 funding from the Engineering and Physical Sciences Research Council (capital grant EP/P020259/1), and DiRAC funding from the Science and Technology Facilities Council (www.dirac.ac.uk). AZ acknowledges financial support from the Leverhulme Trust, grant number RPG-2020-038.

REFERENCES

[1] A. Fasolino, J. H. Los, and M. I. Katsnelson, Nature Materials **6**, 858 (2007).
[2] H. Qin, Y. Sun, J. Z. Liu, and Y. Liu, Carbon **108**, 204 (2016).
[3] F. Guinea, B. Horovitz, and P. Le Doussal, Physical Review B - Condensed Matter and Materials Physics **77**, 205421 (2008).
[4] F. Guinea, M. I. Katsnelson, and M. A. Vozmediano, Physical Review B - Condensed Matter and Materials Physics **77**, 075422 (2008).
[5] A. L. Vázquez De Parga, F. Calleja, B. Borca, M. C. Passeggi, J. J. Hinarejos, F. Guinea, and R. Miranda, Physical Review Letters **100**, 056807 (2008).
[6] D. W. Boukhvalov and M. I. Katsnelson, Journal of Physical Chemistry C **113**, 14176 (2009).
[7] L. Qiu, X. Zhang, W. Yang, Y. Wang, G. P. Simon, and D. Li, Chemical Communications **47**, 5810 (2011).
[8] N. Wei, C. Lv, and Z. Xu, Langmuir **30**, 3572 (2014).
[9] M. Dahanayaka, B. Liu, Z. Hu, Z. Chen, A. W. K. Law, and K. Zhou, Physical Chemistry Chemical Physics **19**, 8552 (2017).
[10] S. Marbach, D. S. Dean, and L. Bocquet, Nature Physics **14**, 1108 (2018).
[11] P. O. Lehtinen, A. S. Foster, A. Ayuela, A. Krasheninnikov, K. Nordlund, and R. M. Nieminen, Physical Review Letters **91**, 017202 (2003).
[12] M. Sammalkorpi, A. Krasheninnikov, A. Kuronen, K. Nordlund, and K. Kaski, Physical Review B - Condensed Matter and Materials Physics **70**, 245416 (2004).
[13] R. N. Costa Filho, G. A. Farias, and F. M. Peeters, Physical Review B - Condensed Matter and Materials Physics **76**, 193409 (2007).
[14] S. V. Kopylov, V. Cheianov, B. L. Altshuler, and V. I. Fal'Ko, Physical Review B - Condensed Matter and Materials Physics **83**, 201401(R) (2011).
[15] M. C. Wang, C. Yan, L. Ma, N. Hu, and M. W. Chen, Computational Materials Science **54**, 236 (2012).
[16] R. Ansari, S. Ajori, and B. Motevalli, Superlattices and Microstructures **51**, 274 (2012).
[17] B. Mortazavi and S. Ahzi, Carbon **63**, 460 (2013).
[18] L. He, S. Guo, J. Lei, Z. Sha, and Z. Liu, Carbon **75**, 124 (2014).
[19] A. Zandiatashbar, G. H. Lee, S. J. An, S. Lee, N. Mathew, M. Terrones, T. Hayashi, C. R. Picu, J. Hone, and N. Koratkar, Nature Communications **5**, 3186 (2014).
[20] Y. Wei, J. Wu, H. Yin, X. Shi, R. Yang, and M. Dresselhaus, Nature Materials **11**, 759 (2012).
[21] D. W. Boukhvalov and M. I. Katsnelson, Nano Letters **8**, 4373 (2008).
[22] F. Banhart, J. Kotakoski, and A. V. Krasheninnikov, ACS Nano **5**, 26 (2011).
[23] R. R. Nair, M. Sepioni, I. L. Tsai, O. Lehtinen, J. Keinonen, A. V. Krasheninnikov, T. Thomson, A. K. Geim, and I. V. Grigorieva, Nature Physics **8**, 199 (2012).
[24] H. Malekpour, P. Ramnani, S. Srinivasan, G. Balasubramanian, D. L. Nika, A. Mulchandani, R. K. Lake, and A. A. Balandin, Nanoscale **8**, 14608 (2016).

[25] A. M. Valencia and M. J. Caldas, Physical Review B **96**, 125431 (2017).
[26] E. Griffin, L. Mogg, G. P. Hao, G. P. Hao, G. Kalon, G. Kalon, C. Bacaksiz, G. Lopez-Polin, G. Lopez-Polin, T. Y. Zhou, V. Guarochico, J. Cai, C. Neumann, A. Winter, M. Mohn, J. H. Lee, J. Lin, J. Lin, U. Kaiser, I. V. Grigorieva, K. Suenaga, B. Özyilmaz, H. M. Cheng, H. M. Cheng, W. Ren, A. Turchanin, F. M. Peeters, A. K. Geim, and M. Lozada-Hidalgo, ACS Nano **14**, 7280 (2020).
[27] S. Hu, M. Lozada-Hidalgo, F. C. Wang, A. Mishchenko, F. Schedin, R. R. Nair, E. W. Hill, D. W. Boukhvalov, M. I. Katsnelson, R. A. Dryfe, I. V. Grigorieva, H. A. Wu, and A. K. Geim, Nature **516**, 227 (2014).
[28] P. Z. Sun, Q. Yang, W. J. Kuang, Y. V. Stebunov, W. Q. Xiong, J. Yu, R. R. Nair, M. I. Katsnelson, S. J. Yuan, I. V. Grigorieva, M. Lozada-Hidalgo, F. C. Wang, and A. K. Geim, Nature **579**, 229 (2020).
[29] M. T. Lusk and L. D. Carr, Physical Review Letters **100**, 175503 (2008).
[30] A. V. Krasheninnikov and F. Banhart, Nature Materials **6**, 723 (2007).
[31] A. V. Krasheninnikov, K. Nordlund, M. Sirviö, and J. Salonen, E.Keinonen, Physical Review B - Condensed Matter and Materials Physics **63**, 245405 (2001).
[32] J. Kotakoski, A. V. Krasheninnikov, U. Kaiser, and J. C. Meyer, Physical Review Letters **106**, 105505 (2011).
[33] J. Kotakoski, J. C. Meyer, S. Kurasch, D. Santos-Cottin, U. Kaiser, and A. V. Krasheninnikov, Physical Review B - Condensed Matter and Materials Physics **83**, 245420 (2011).
[34] A. W. Robertson, C. S. Allen, Y. A. Wu, K. He, J. Olivier, J. Neethling, A. I. Kirkland, and J. H. Warner, Nature Communications **3**, 1144 (2012).
[35] T. Susi, J. C. Meyer, and J. Kotakoski, Ultramicroscopy **180**, 163 (2017).
[36] X. Zhao, J. Kotakoski, J. C. Meyer, E. Sutter, P. Sutter, A. V. Krasheninnikov, U. Kaiser, and W. Zhou, MRS Bulletin **42**, 667 (2017).
[37] M. Tripathi, A. Mittelberger, N. A. Pike, C. Mangler, J. C. Meyer, M. J. Verstraete, J. Kotakoski, and T. Susi, Nano Letters **18**, 5319 (2018).
[38] A. Trentino, J. Madsen, A. Mittelberger, C. Mangler, T. Susi, K. Mustonen, and J. Kotakoski, Nano Letters **21**, 5179 (2021).
[39] O. V. Yazyev, I. Tavernelli, U. Rothlisberger, and L. Helm, Physical Review B - Condensed Matter and Materials Physics **75**, 115418 (2007).
[40] K. Yoon, A. Rahnamoun, J. L. Swett, V. Iberi, D. A. Cullen, I. V. Vlassiouk, A. Belianinov, S. Jesse, X. Sang, O. S. Ovchinnikova, A. J. Rondinone, R. R. Unocic, and A. C. Van Duin, ACS Nano **10**, 8376 (2016).
[41] T. Shi, Q. Peng, Z. Bai, F. Gao, and I. Jovanovic, Nanoscale **11**, 20754 (2019).
[42] S. Su and J. Xue, ACS Applied Materials and Interfaces **13**, 12366 (2021).
[43] Y. Zhu, S. Murali, M. D. Stoller, K. J. Ganesh, W. Cai, P. J. Ferreira, A. Pirkle, R. M. Wallace, K. A. Cychosz, M. Thommes, D. Su, E. A. Stach, and R. S. Ruoff, Science **332**, 1537 (2011).
[44] J. Wang, B. Chen, and B. Xing, Environmental Science and Technology **50**, 3798 (2016).
[45] W. Bao, F. Miao, Z. Chen, H. Zhang, W. Jang, C. Dames, and C. N. Lau, Nature Nanotechnology **4**, 562 (2009).
[46] C. T. Toh, H. Zhang, J. Lin, A. S. Mayorov, Y. P. Wang, C. M. Orofeo, D. B. Ferry, H. Andersen, N. Kakenov, Z. Guo, I. H. Abidi, H. Sims, K. Suenaga, S. T. Pantelides, and B. Özyilmaz, Nature **577**, 199 (2020).
[47] T. Zhao, C. Xu, W. Ma, Z. Liu, T. Zhou, Z. Liu, S. Feng, M. Zhu, N. Kang, D. M. Sun, H. M. Cheng, and W. Ren, Nature Communications **10**, 4854 (2019).
[48] V. Tozzini and V. Pellegrini, Journal of Physical Chemistry C **115**, 25523 (2011).
[49] J. Guo, J. R. Morris, Y. Ihm, C. I. Contescu, N. C. Gallego, G. Duscher, S. J. Pennycook, and M. F. Chisholm, Small **8**, 3283 (2012).
[50] Y. Ito, Y. Shen, D. Hojo, Y. Itagaki, T. Fujita, L. Chen, T. Aida, Z. Tang, T. Adschiri, and M. Chen, Advanced Materials **28**, 10644 (2016).
[51] J. Wang, Z. Chen, and B. Chen, Environmental Science and Technology **48**, 4817 (2014).
[52] O. Glukhova and M. Slepchenkov, Nanoscale **4**, 3335 (2012).
[53] X. Chen and B. Chen, Environmental Science and Technology **49**, 6181 (2015).
[54] J. G. Radich and P. V. Kamat, ACS Nano **7**, 5546 (2013).
[55] H. Terrones and A. L. Mackay, Carbon **30**, 1251 (1992).
[56] W. T. Irvine, V. Vitelli, and P. M. Chaikin, Nature **468**, 947 (2010).
[57] Y. Liu and B. I. Yakobson, Nano Letters **10**, 2178 (2010).
[58] K. Kawasumi, Q. Zhang, Y. Segawa, L. T. Scott, and K. Itami, Nature Chemistry **5**, 739 (2013).
[59] H. Kusumaatmaja and D. J. Wales, Physical Review Letters **110**, 165502 (2013).
[60] M. Brojan, D. Terwagne, R. Lagrange, and P. M. Reis, Proceedings of the National Academy of Sciences of the United States of America **112**, 14 (2015).
[61] J. H. Warner, Y. Fan, A. W. Robertson, K. He, E. Yoon, and G. D. Lee, Nano Letters **13**, 4937 (2013).
[62] O. Lehtinen, S. Kurasch, A. V. Krasheninnikov, and U. Kaiser, Nature Communications **4**, 2098 (2013).
[63] S. K. Jain, G. T. Barkema, N. Mousseau, C. M. Fang, and M. A. Van Huis, Journal of Physical Chemistry C **119**, 9646 (2015).
[64] H. C. Schniepp, K. N. Kudin, J. L. Li, R. K. Prud'Homme, R. Car, D. A. Saville, and I. A. Aksay, ACS Nano **2**, 2577 (2008).
[65] J. Kotakoski, F. R. Eder, and J. C. Meyer, Physical Review B - Condensed Matter and Materials Physics **89**, 201406(R) (2014).
[66] G. G. Samsonidze, G. G. Samsonidze, and B. I. Yakobson, Computational Materials Science **23**, 62 (2002).
[67] Z. Pang, B. Deng, Z. Liu, H. Peng, and Y. Wei, Carbon **143**, 736 (2019).
[68] O. Lehtinen, N. Vats, G. Algara-Siller, P. Knyrim, and U. Kaiser, Nano Letters **15**, 235 (2015).
[69] O. V. Yazyev and S. G. Louie, Physical Review B - Condensed Matter and Materials Physics **81**, 195420 (2010).
[70] T. H. Liu, G. Gajewski, C. W. Pao, and C. C. Chang, Carbon **49**, 2306 (2011).
[71] C. Hofer, C. Kramberger, M. R. A. Monazam, C. Mangler, A. Mittelberger, G. Argentero, J. Kotakoski, and J. C. Meyer, 2D Materials **5**, 045029 (2018).
[72] J. H. Warner, E. R. Margine, M. Mukai, A. W. Robertson, F. Giustino, and A. I. Kirkland, Science **337**, 209 (2012).
[73] C. G. Wang, L. Lan, Y. P. Liu, and H. F. Tan, Computational Materials Science **77**, 250 (2013).
[74] T. Zhang, X. Li, and H. Gao, Journal of the Mechanics and Physics of Solids **67**, 2 (2014).
[75] T. Zhang, X. Li, and H. Gao, Extreme Mechanics Letters **1**, 3 (2014).
[76] G. López-Polín, C. Gómez-Navarro, V. Parente, F. Guinea, M. I. Katsnelson, F. Pérez-Murano, and J. Gómez-Herrero, Nature Physics **11**, 26 (2014).
[77] G. López-Polín, M. Ortega, J. G. Vilhena, I. Alda, J. Gomez-Herrero, P. A. Serena, C. Gomez-Navarro, and R. Pérez, Carbon **116**, 670 (2017).
[78] A. W. Robertson and J. H. Warner, Nanoscale **5**, 4079 (2013).
[79] S. T. Skowron, I. V. Lebedeva, A. M. Popov, and E. Bichoutskaia, Chemical Society Reviews **44**, 3143 (2015).
[80] A. J. Stone and D. J. Wales, Chemical Physics Letters **128**, 501 (1986).
[81] Y. Kim, J. Ihm, E. Yoon, and G. D. Lee, Physical Review B - Condensed Matter and Materials Physics **84**, 075445 (2011).

[82]F. L. Thiemann, P. Rowe, E. A. Müller, and A. Michaelides, The Journal of Physical Chemistry C **124**, 22278 (2020).
[83]H. Los and A. Fasolino, Physical Review B - Condensed Matter and Materials Physics **68**, 024107 (2003).
[84]S. J. Stuart, A. B. Tutein, and J. A. Harrison, Journal of Chemical Physics **112**, 6472 (2000).
[85]N. A. Marks, Physical Review B - Condensed Matter and Materials Physics **63**, 035401 (2001).
[86]P. Rowe, V. L. Deringer, P. Gasparotto, G. Csányi, and A. Michaelides, Journal of Chemical Physics **153**, 034702 (2020).
[87]A. P. Bartók, M. C. Payne, R. Kondor, and G. Csányi, Physical Review Letters **104**, 136403 (2010).
[88]A. P. Bartók and G. Csányi, International Journal of Quantum Chemistry **115**, 1051 (2015).
[89]J. C. Meyer, C. Kisielowski, R. Erni, M. D. Rossell, M. F. Crommie, and A. Zettl, Nano Letters **8**, 3582 (2008).
[90]I. C. Gerber, A. V. Krasheninnikov, A. S. Foster, and R. M. Nieminen, New Journal of Physics **12**, 113021 (2010).
[91]S. Plimpton, Journal of Computational Physics **117**, 1 (1995).
[92]A. Hjorth Larsen, J. JØrgen Mortensen, J. Blomqvist, I. E. Castelli, R. Christensen, M. Dułak, J. Friis, M. N. Groves, B. Hammer, C. Hargus, E. D. Hermes, P. C. Jennings, P. Bjerre Jensen, J. Kermode, J. R. Kitchin, E. Leonhard Kolsbjerg, J. Kubal, K. Kaasbjerg, S. Lysgaard, J. Bergmann Maronsson, T. Maxson, T. Olsen, L. Pastewka, A. Peterson, C. Rostgaard, J. SchiØtz, O. Schütt, M. Strange, K. S. Thygesen, T. Vegge, L. Vilhelmsen, M. Walter, Z. Zeng, and K. W. Jacobsen, Journal of Physics Condensed Matter **29**, 273002 (2017).
[93]N. Michaud-Agrawal, E. J. Denning, T. B. Woolf, and O. Beckstein, Journal of computational chemistry **32**, 2319 (2011).
[94]R. Gowers, M. Linke, J. Barnoud, T. Reddy, M. Melo, S. Seyler, J. Domański, D. Dotson, S. Buchoux, I. Kenney, and O. Beckstein, Proceedings of the 15th Python in Science Conference , 98 (2016).
[95]A. Stukowski, Modelling and Simulation in Materials Science and Engineering **18**, 015012 (2010).
[96]D. R. Nelson and L. Peliti, Journal de physique Paris **48**, 1085 (1987).
[97]P. Le Doussal and L. Radzihovsky, Physical Review Letters **69**, 1209 (1992).
[98]D. R. Nelson, T. Piran, and S. Weinberg, eds., *Statistical Mechanics of Membranes and Surfaces*, 2nd ed. (World Scientific, Singapore, 2004).
[99]P. Rowe, G. Csányi, D. Alfè, and A. Michaelides, Physical Review B **97**, 054303 (2018).
[100]J. Ma, D. Alfè, A. Michaelides, and E. Wang, Physical Review B - Condensed Matter and Materials Physics **80**, 033407 (2009).
[101]J. M. Leyssale and G. L. Vignoles, Journal of Physical Chemistry C **118**, 8200 (2014).
[102]M. Ma, G. Tocci, A. Michaelides, and G. Aeppli, Nature Materials **15**, 66 (2016).
[103]D. Odkhuu, D. H. Jung, H. Lee, S. S. Han, S. H. Choi, R. S. Ruoff, and N. Park, Carbon **66**, 39 (2014).

Supporting Information for: Defect-Dependent Corrugation in Graphene

Fabian L. Thiemann[1,2,3,4], Patrick Rowe[1,2,3], Andrea Zen[5,6,2], Erich A. Müller[4], and Angelos Michaelides[3,1,2]

[1]Department of Physics and Astronomy, University College London, Gower Street, London, WC1E 6BT, United Kingdom
[2]Thomas Young Centre and London Centre for Nanotechnology, University College London, Gower Street, London, WC1E 6BT, United Kingdom
[3]Yusuf Hamied Department of Chemistry, University of Cambridge, Lensfield Road, Cambridge, CB2 1EW, United Kingdom
[4]Department of Chemical Engineering, Imperial College London, South Kensington Campus, London SW7 2AZ, United Kingdom
[5]Dipartimento di Fisica Ettore Pancini, Università di Napoli Federico II, Monte S. Angelo, I-80126 Napoli, Italy
[6]Department of Earth Sciences, University College London, Gower Street, London WC1E 6BT, United Kingdom

In this supplementary information, we provide additional details on certain aspects of the study reported in the manuscript. This includes a comprehensive summary of the computational details and methods, additional results mentioned in the manuscript, as well as an analysis of the dependence of the results on simulation time and defect arrangement.

1 Details of the molecular dynamics simulations

In our classical molecular dynamics (MD) simulations, the system size varied dependent on defect concentration between 6984 and 7200 atoms. We employed monoclinic simulation cells where the length of the inplane lattice vectors was $\approx$ 14.6 nm. Periodic boundary conditions were applied in all three directions. We prevented the graphene sheet from interacting with its periodic images in the direction normal to the surface by adding 4 nm of vacuum which is way beyond the cutoff of the GAP-20 [1] (1 nm). In case of the defective systems, the defects were randomly distributed on the sheet while satisfying a minimum distance criterion of 1 nm between the defect centers. Similarly, the orientation of each defect was assigned randomly.

A timestep of 1 fs was used and all simulations were performed at 300 K and zero strain in the isobaric-isothermal ensemble (NPT). To ensure target temperature and stress, we employed a Nosé-Hoover chain thermostat and barostat. Notably, the barostat was only applied to the in-plane dimensions which were also coupled to each other to guarantee graphene remains of hexagonal nature. We equilibrated each system for 20 ps before collecting statistics for at least 150 ps. In this supplementary material, we show that this relatively short production time is sufficient to accurately sample the properties presented in the manuscript. All molecular dynamics (MD) simulations reported in the manuscript were performed in LAMMPS [2].

2 Definition of the corrugation amplification factor

In the manuscript, we introduced the corrugation amplification factor (CAF) to quantify the impact of defects on the structure of graphene. Here, we provide

a detailed explanation of how this measure is computed. As explained in the manuscript, the CAF represents the ratio of the standard deviation of the atomic heights distribution between defective and pristine graphene. Therefore, we start by defining the atomic height $h_{i,j}$ as the out-of-plane displacement (in z-direction) of an atom i at simulation frame j from the center of geometry (equivalent to center of mass for graphene) of the system,

$$h_{i,j} = z_{i,j} - \sum_{i}^{N_{\text{atoms}}} z_{i,j} \ , \tag{1}$$

where $z_{i,j}$ represents the z-coordinate of atom i at frame j and N_{atoms} corresponds to the total number of atoms. We compute $h_{i,j}$ for all atoms in the system and for all frames N_{frames} of the trajectory and determine the standard deviation s_h of this atomic height distribution

$$s_h = \sqrt{\frac{1}{N_{\text{frames}} N_{\text{atoms}}} \sum_{j}^{N_{\text{frames}}} \sum_{i}^{N_{\text{atoms}}} \left(h_{i,j} - \bar{h}\right)^2} \ , \tag{2}$$

where $\bar{h}$ is the mean atomic height given by

$$\bar{h} = \frac{1}{N_{\text{frames}} N_{\text{atoms}}} \sum_{j}^{N_{\text{frames}}} \sum_{i}^{N_{\text{atoms}}} h_{i,j} \ . \tag{3}$$

The standard deviation s_h represents a quantitative measure of the corrugation of the system where large values correspond to a highly corrugated graphene sheet. In order evaluate the impact of defects on graphene's structure, we use the CAF which expresses s_h of a defective system relative to the standard deviation measured for pristine graphene

$$\text{CAF} = \frac{s_h^{\text{defective}}}{s_h^{\text{pristine}}} \ . \tag{4}$$

3 Analysis of the defects' local environments

To understand the distinct corrugation induced by different defect types we computed the inclination and Gaussian curvature of the defects' local environments and compared them to the representative values in pristine graphene. Here, we provide a comprehensive summary of this approach. At first, we identified all atoms within a distance of 4.5 Å, corresponding to the cutoff of the many-body SOAP descriptor used by the GAP-20 [1], from the center of mass of a defect. For pristine graphene, the artificial defect centers were randomly assigned to individual carbon atoms obeying the minimum distance criterion described in the previous section. The selected atoms form the local environments of a defect varying in number between 22 and 25 dependent on the defect type as illustrated in figure S1.

Next, we computed the orientation of each defect with respect to a previously defined reference indicated in figure S1. For Stone-Wales and divacancy defects, the x-axis was assigned along the axis connecting the 5-membered rings whereas the y-axis was parallel to the heptagons and octagon, respectively. For the pristine case where three hexagons form an artificial defect, the local y-axis was assigned to point from the defect center towards the two hexagons in the global y-direction.

Having defined the local environments and their respective orientation for all defects in the system, we looped through the trajectories to compute the geometrical parameters in the following manner: For every defect in each frame, we expressed the coordinates of the atoms forming the local environment relative to the center of mass of the defect. To enable a comparison between defects of different orientation, we rotated the local coordinates around the local z-axis at the defect center to arrange all of them in the same reference orientation shown

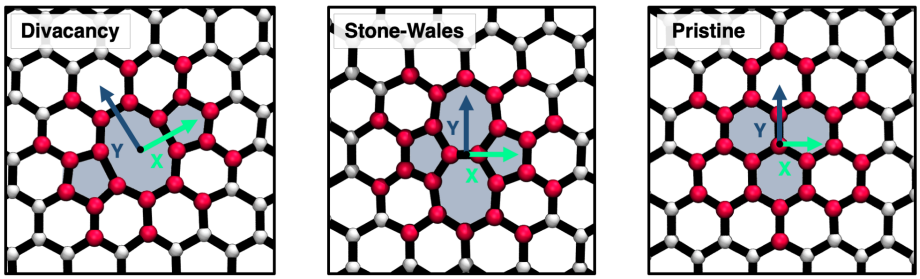

Figure S1: Overview of the local environments for the different defect types. The N-membered rings forming the defects are highlighted in greyish blue. Atoms assigned to a defect are coloured in red while all other atoms are illustrated in light grey. The reference orientation for each defect type are indicated by the local coordinate system anchored at the defect center.

in figure S1. Then, a two-dimensional second-order equation,

$$f_h(x,y) = a + bx + cy + dxy + ex^2 + fy^2 \ , \tag{5}$$

was fitted to the relative heights of the translated and rotated atom coordinates. If the quality of the fit was sufficiently accurate, i.e. the R^2 score was above 0.9, first and second derivatives of the analytical function at the defect's center of mass, corresponding to (0,0) in the local coordinate system, were computed. Notably, almost all fits (> 99.9 %) satisfied our accuracy criterion suggesting that a second-order equation can adequately describe the local environments. Based on the definition of $f_h(x,y)$, the gradient ∇f_h and Hessian $\mathbf{H}$ at (0,0) are readily obtained:

$$\nabla f_h(0,0) = \begin{bmatrix} \frac{\partial f_h(x,y)}{\partial x}|_{x=y=0} \\ \frac{\partial f_h(x,y)}{\partial y}|_{x=y=0} \end{bmatrix} = \begin{bmatrix} b \\ c \end{bmatrix} \tag{6}$$

$$\mathbf{H}(0,0) = \begin{bmatrix} \frac{\partial^2 f_h(x,y)}{\partial x^2}|_{x=y=0} & \frac{\partial^2 f_h(x,y)}{\partial x \partial y}|_{x=y=0} \\ \frac{\partial^2 f_h(x,y)}{\partial y \partial x}|_{x=y=0} & \frac{\partial^2 f_h(x,y)}{\partial y^2}|_{x=y=0} \end{bmatrix} = \begin{bmatrix} 2e & d \\ d & 2f \end{bmatrix} . \tag{7}$$

As last step, we computed the norm of the gradient, $\nabla f_h(0,0)$, and the determinant of the Hessian, $\mathbf{H}(0,0)$, to obtain the local inclination and Gaussian curvature, respectively. The entire post-processing analysis was done in Python employing commonly used packages such ASE [3], MDAnalysis [4, 5], and OVITO[6].

4 Validation of the GAP-20 for high defect concentrations

While a comprehensive benchmarking of the GAP-20 [1] and a detailed comparison to other established force fields can be found in the original reference, here we report the performance of the potential for highly defective and corrugated graphene with respect to its density functional theory (DFT) reference. To this end, we computed the deviation in the atomic forces between DFT and GAP for a set of reference configurations. These structures were taken from 6 MD simulations based on the GAP-20 of defective graphene with up to 200 atoms comprising between one and three defects (corresponding to defect concentrations of 1 % and 3 %, respectively) of either Stone-Wales or divacancy character. All MD simulations were performed using the same settings as reported above. For the DFT calculations we used the identical code and setup employed for the generation of the training data for the GAP-20 [1]. Overall, we randomly selected 20 frames from each trajectory to obtain a test set of 120 configurations. In figure S2 we show the correlation of the forces subdivided into the different types and number of defects. Generally, we find smaller root mean square error (RMSE) for systems comprising Stone-Wales defects rather than divacancies. Moreover, the RMSE increases for both types when more defects are added reaching its maximum for the system with three divacancy defects at

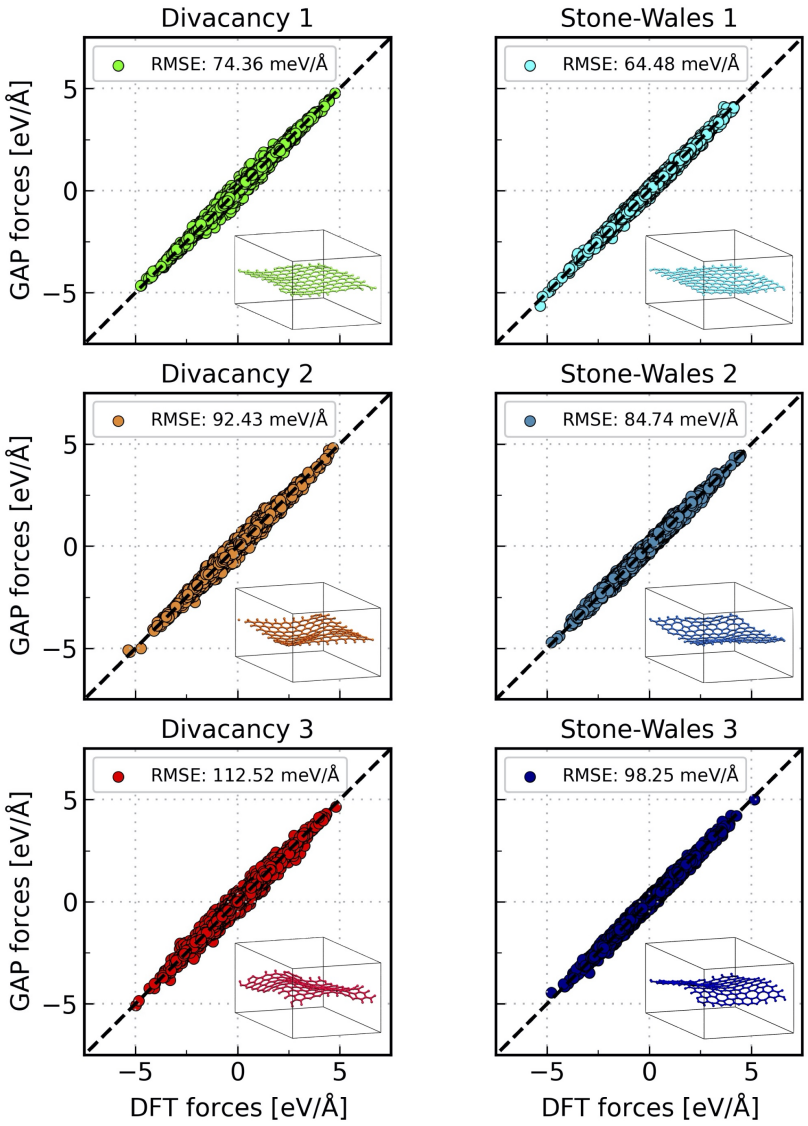

Figure S2: Correlation between the atomic forces predicted by GAP-20 and its DFT reference for a variety of systems. Systems comprising divacancy defects are shown in the left column of plots while the right column is dedicated to Stone-Wales defects. The number of defects increases from 1 at the top panel to 3 at the bottom panel. The inset in each plots pictures a snapshot of a representative configuration in the test set of the respective system. The root mean square error (RMSE) is shown at the top of each plot.

≈ 113 meV/Å. These observations indicate that systems comprising a high corrugation are more challenging to describe for the GAP-20 than those exhibiting an almost flat and smooth topology. It is noteworthy, however, that the magnitude of the force error for all systems is relatively small and comparable to the RMSE found for the recently developed GAP for hexagonal boron nitride in our previous work [7]. This suggests that the GAP-20 is able to provide an accurate description also in the presence of high corrugation.

5 Convergence with respect to simulation time

The wide range of defect concentrations covered by this work and the relative high computational cost associated with the GAP-20 [1] impose a limit to the length of each simulation for the system sizes studied here. Therefore, most results presented in the manuscript are based on trajectories of a production length of 150 ps. In this section, we show that our results based on short simulation time agree well with those obtained from a significantly longer trajectory. To this end, we analyse the dependence of the structural properties reported in the manuscript, i.e. the standard deviation of the atomic height distribution as well as the local geometrical parameters, on the simulation time. By showing the standard deviation of the atomic height distribution rather than the corrugation amplification factor (CAF), we are able to also analyse the convergence for the pristine sheet. For both defect types, this analysis is carried out at a defect concentration of ≈ 0.06 % (corresponding to two defects) and 1 % where we elongated individual trajectories.

A summary of this convergence analysis is shown in figure S3. For all properties, the qualitative difference between the pristine and the highly defective systems is apparent irrespective of the simulation time. In general, the properties of the less defective systems converge way quicker than the equivalent for

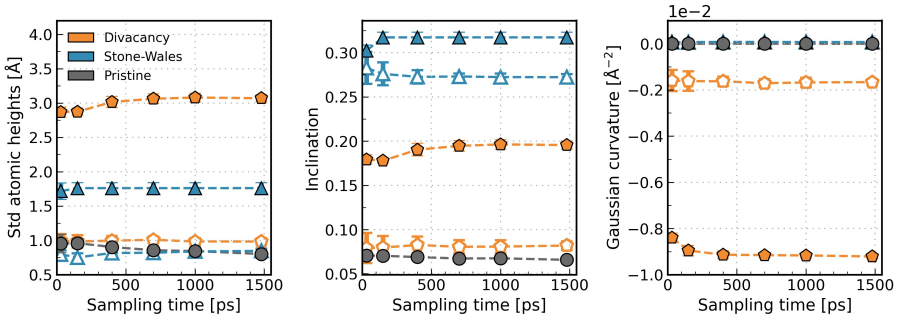

Figure S3: Analysis of the convergence of structural properties with respect to sampling time. The properties investigated include the standard deviation of the atomic height distribution (left), the local inclination (center), and the local Gaussian curvature (right) of the local environments around defects. The markers represent the computed properties where the filled and the lines serve as guide to the eye. For the defective systems, the filled symbols correspond to a defect concentration of 1 % while the empty ones illustrate properties for systems comprising two defects only. The statistical error visualised by the error bars was computed based on block averages using 20 blocks.

the higher defect concentration. We therefore focus on the high defect concentration in our discussion and compare the distinct trends in the dependence of the simulation time for the different systems. For graphene comprising Stone-Wales defects, the geometrical parameters converge rapidly while the standard deviation of the atomic heights takes considerably longer although the results obtained based on a shorter sampling time are within the statistical error of the longest simulation time of 1.5 ns. Divacancy systems show a slow convergence for all structural properties analysed agreeing, however, within 8 % with results obtained from longer simulation times. Pristine graphene converges rapidly for the geometrical parameters describing the local environments, while a longer simulation times are required to achieve convergence for the standard deviation of the atomic height distribution. Based on these findings, we conclude that our results are sufficiently converged within 150 ps to allow for a qualitative comparison between the different systems.

6 Convergence with respect to system size

Similar to the constrains on the accessible simulation times, the high computational cost associated with the GAP-20 also restrict the system sizes feasible for a scan of different defect types at varying concentrations. In this work, we chose a system size corresponding to 7200 atoms for the pristine graphene sheet equivalent to our previous work on strain-induced rippling in two-dimensional materials [7]. It is worth noting, however, that the height fluctuations in graphene scale with the spatial dimensions of the system [8–10]. Here, we analyse the dependence of the CAF on the system size by performing MD simulations on systems comprising 1800 and 5000 atoms, respectively. We use the identical setup and simulation times as described in the manuscript, namely 150 ps and 1 ns for defective and pristine systems, respectively. However, we restrict our analysis of the size dependence of the CAF to a defect concentration of 1% for both defect types. For each size, we conducted three independent simulations varying the spatial arrangement of the defects.

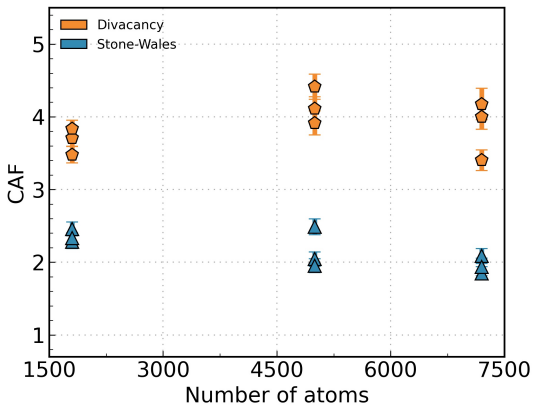

Figure S4: Analysis of the convergence of CAF with respect to system size. The markers represent the computed properties and the lines serve as guide to the eye. The statistical error visualised by the error bars was computed based on block averages using 20 blocks.

In figure S4 we show the CAF as function of the number of atoms of the respective pristine systems. Although divacancies and Stone-Wales defects show opposite trends for the CAF with increasing system size, this dependence on the number of atoms is fairly small. In fact, the magnitude of the variation of the CAF with system size is smaller than the range of values observed for different spatial arrangements of defects on the graphene sheet.

7 Impact of defect arrangement on results

It has been shown that the arrangement and orientation of defects has a high impact on the corrugation of graphene [11–13]. In the manuscript, we therefore report the structural properties based on three different defect distributions for each defect type at every concentration. Here, we show that this is a sufficiently large number to estimate the scattering width of our results due to different defect arrangements on the graphene sheet.

For both defect types, we extended our set of defect distributions from three to five for three different concentrations to also account for a varying effect based on the number of defects present. These systems include a low ($\approx$ 0.06 %), high (1 %), and very high (3 %) defect concentration. Similar to the convergence analysis with respect to the simulation time, we computed all structural properties reported in the manuscript and summarised the results in figure S5. Irrespective of the defect type, property, and concentration, we find that the additionally performed simulations fall within the range of values reported in the manuscript. Therefore, we conclude that performing simulations with three different defect distributions is sufficient to make general statements about the distinct impact of different defect types.

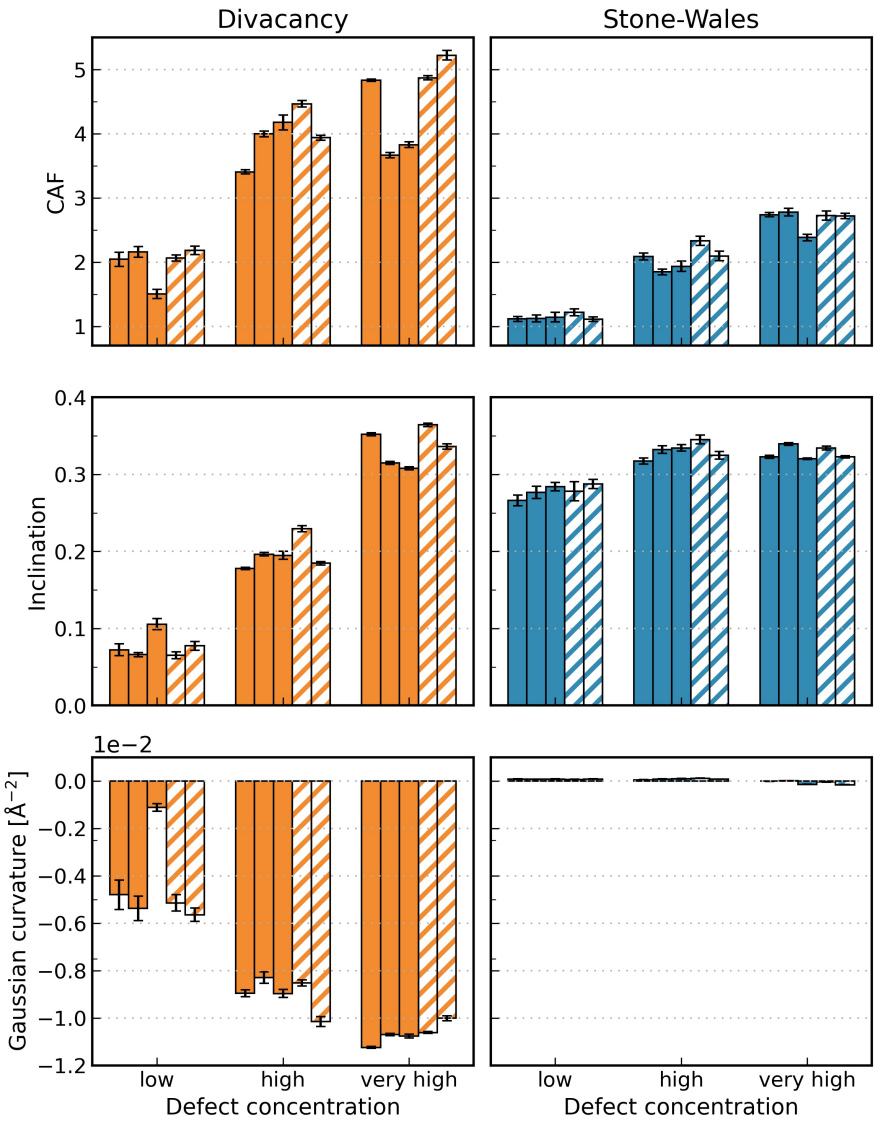

Figure S5: Impact of different defect distributions on graphene's structural properties investigated in this work for both defect types. Results presented in the manuscript are visualised by single-coloured bars while the additionally performed simulations are illustrated by hatched bars. The statistical error visualised by the error bars was computed based on block averages using 20 blocks. For all systems comprising Stone-Wales defects the Gaussian curvature is approximately zero.

8 Dependence of the lattice parameter on the defect concentration

As we perform our MD simulations with a varying box size, it is interesting to compare the impact of the increasing defect concentration on the lattice parameter of graphene. For all simulations reported in the manuscript, we computed the average lattice parameter and show their values relative to pristine graphene ($a_{\mathrm{pristine}} = 2.462$ Å) in figure S6. As expected, the lattice parameter decreases with increasing defect concentration due to the significantly higher out-of-plane deviations. While there is some scattering between different defect distributions for the divacancies, the two types compared are clearly distinguishable as predicted by their distinct CAFs. For the highest concentrations investigated (3 %), systems comprising Stone-Wales defects and divacancies show a lattice parameter reduced by ≈ 2 % and ≈ 5 %, respectively.

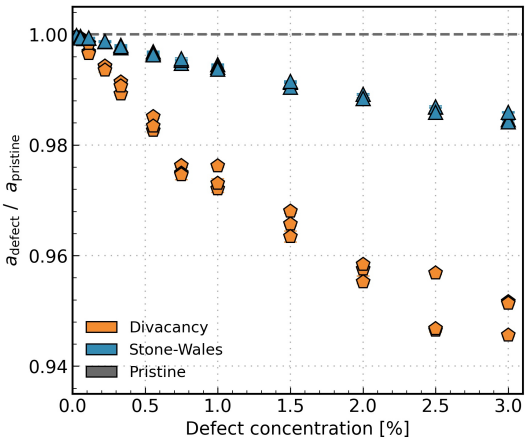

Figure S6: Lattice parameter of defective graphene expressed relative to pristine graphene as function of the defect concentration. The statistical error visualised by the error bars was computed based on block averages using 20 blocks.

9 Comparison between reconstructed divacancies

In the manuscript, we compare the morphological impact of Stone-Wales defects and divacancies, where the latter comprises one 8-membered and two 5-membered rings. In this section of the supplementary material, we, thus, refer to this defect as V_2 (5-8-5). However, experiments [14] confirm the existence of two additional states of reconstructed divacancies which can arise from V_2 (5-8-5) through the additional rotation of one and two C-C bonds, respectively. While one of these Stone-Wales-like transformations leads to the formation of 3 pentagons and 3 heptagons, termed V_2 (555-777), two bond rotations create four 5-membered, one 6-membered, and four 7-membered rings to which we refer as V_2 (5555-6-7777). All of these defects are illustrated in figure S7 where the different geometrical shapes are also highlighted.

Here, we compare the morphological impact between these different types of divacancies. To this end, we performed additional MD simulations of graphene comprising V_2 (555-777) and V_2 (5555-6-7777) defects and compute the CAF. Rather than scanning the entire concentration range, however, we restrict ourselves to the concentrations of 0.5, 1.0. 2.0, and 3.0% for each of which we

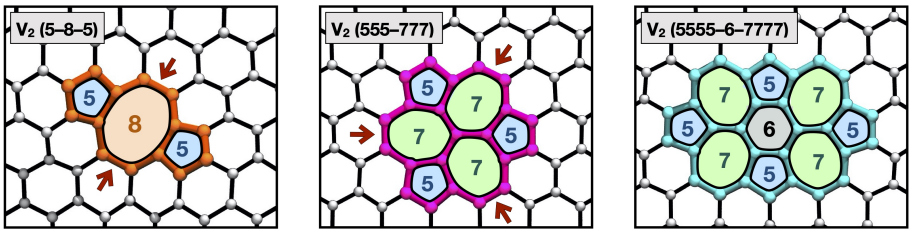

Figure S7: Overview of different states of reconstructed divacancies. For each defect, the differently sized carbon rings are coloured and labeled according to the number of members. In the left and center panels, the red arrows highlight the C-C bonds which are rotated to transform the V_2 (5-8-5) to the V_2 (555-777) and the V_2 (555-777) to the V_2 (5555-6-7777), respectively.

perform three independent simulations per type varying in the spatial arrangement of the defects. While we use the identical simulation setup described above, due to the larger size of these defects we increased the minimum distance between them to 14Å and 17Å for V_2 (555-777) and V_2 (5555-6-7777) defects, respectively. In contrast to V_2 (5-8-5) and Stone-Wales defects where 2 atoms per defect are modified (removed or rotated, respectively), V_2 (555-777) and V_2 (5555-6-7777) defects involve the topological variation of 4 and 6 atoms, respectively, due to the additionally induced bond rotations. Therefore, fewer of these defects are required to achieve a respective defect concentration.

In figure S8 we report the CAF for all three divacancy defects as a function of the defect concentration. As expected, all divacancy defects lead to an enhanced corrugation of graphene. However, our simulations show that additional bond rotations have a strong impact on the magnitude of the corrugation enhancement. While V_2 (5-8-5) defects can induce an up to five times more wrinkled surface at the concentrations investigated, for V_2 (555-777) and V_2 (5555-6-7777) defects we observed a maximum CAF of approximately 2 and 2.75, respectively.

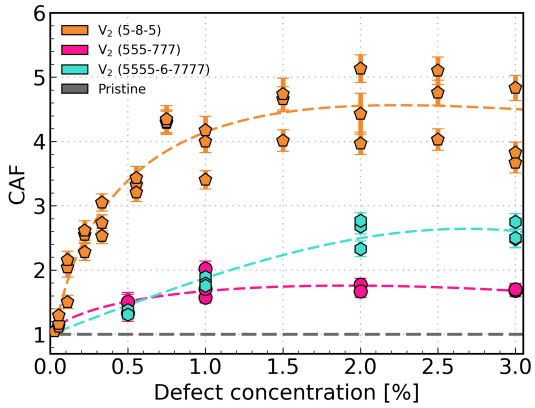

Figure S8: Comparison of the morphological impact of different divacancy defects. The error bars represent the related statistical error obtained via block averaging. The dashed lines are intended as guides to the eye.

This indicates that the impact on graphene's corrugation of the latter two types is rather similar to that one of Stone-Wales defects highlighting the high sensitivity of graphene's morphology with respect to small perturbations such as individual bond rotations.

10 Comparison to graphene under compressive strain

While the focus of this study is the morphological alteration of graphene in the presence of defects, strain represents an alternative approach to increase the system's corrugation [7, 15]. Here, we report the CAF for pristine graphene as a function of strain and compare the corrugation to the defective systems reported in the manuscript. Rather than performing additional simulations, we make use of the trajectories from our previous work [7] where we studied the impact of strain on the amplitude of ripples in graphene and hexagonal boron nitride. This is feasible given the very similar setup including identical number of atoms, temperature and thermostat used in both studies. It is worth pointing out, however, that the simulations in our previous work were performed in the NVT ensemble at each state point (at each strain rate) and were based on the predecessor of the GAP-20, the graphene GAP [16]. While the choice of a constant volume is inevitable for a strain-based study, we also expect a fair comparison between the different potential energy surfaces given that both potentials were trained on the same functional and partially the same set of configurations [1, 16].

We show the dependence of the CAF on strain in figure S9. As expected the surface becomes more corrugated when the system is compressed (negative strain), while positive strain flattens the sheet resulting in a CAF < 1. Under a strong

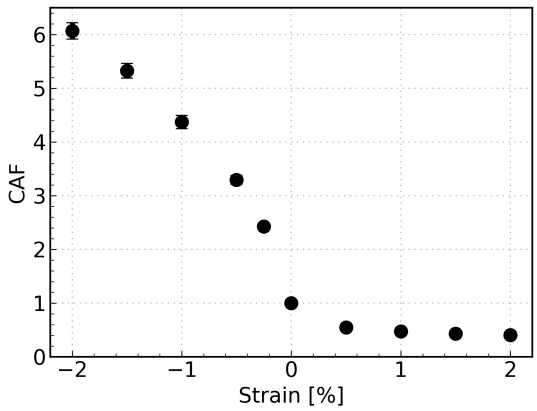

Figure S9: CAF as a function of strain for pristine graphene based on trajectories from reference [7]. Negative and positive strain correspond to compression and tension, respectively. The statistical error visualised by the error bars was computed based on block averages using 20 blocks.

compression of 2 %, the CAF can become as large as ≈ 6 exceeding all the values reported in the manuscript. It is also interesting to note the strong increase of the CAF for low negative strains indicating a high sensitivity of the sheet corrugation to the strain rate.

11 Decomposition of the local inclination

In the manuscript, we characterised the local environments around the defects by means of the local inclination and Gaussian curvature. To get a deeper insight into the preferred configurations of the defects, we can decompose the local inclination into the contributions along the characteristic directions of each defect type described above. Rather than computing the norm of the gradient of the fitted analytical function $f_h(x, y)$ at the origin of the local coordinate system, $\|\nabla f_h(0, 0)\|$, we analyse the absolute spatial derivatives, $|\frac{\partial f_h(x,y)}{\partial x_i}|_{x=y=0}|$, separately.

In figure S10, we show the absolute spatial derivatives in both directions for

all systems investigated in the manuscript. As expected, the individual contributions are essentially identical for pristine graphene indicating the lack of a preferential tilt direction for perfect hexagons. Stone-Wales defects, conversely, show a more complex behaviour which also varies with increasing concentration. For an isolated defect and low defect concentration < 0.25 %, the height gradient mainly appears along the pentagon axis reaching values of ≈ 0.270 while the slope along the heptagon axis (y-direction, see figure S1) remains for most defect arrangements < 0.1. This agrees with *ab initio* calculations [17] showing that the energetically most favourable configuration for a Stone-Wales defect is achieved by displacing the atoms of the pentagon in opposite directions. In case of higher defect concentrations, the gradient along the pentagon axis remains essentially constant through the entire concentration. However, we observe an increase along the heptagon axis plateauing in values of ≈ 0.15 for concentrations > 1.5 %. These findings suggest that the coupling between multiple Stone-Wales defects is mediated through an increase of the gradient

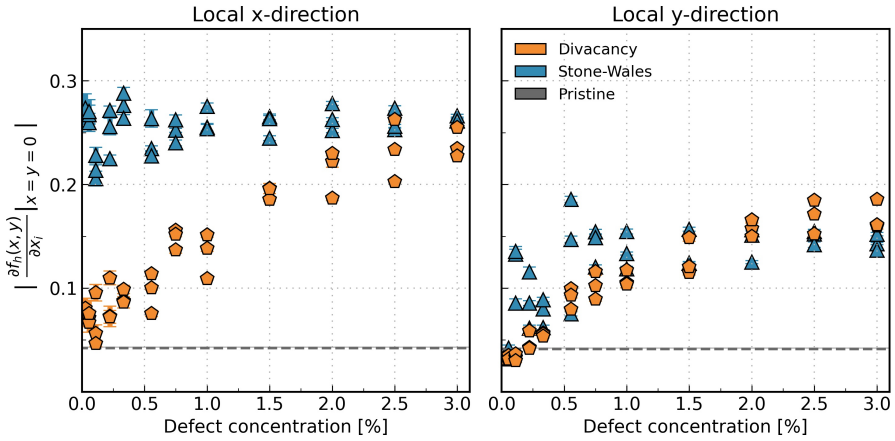

Figure S10: Decomposition of the local inclination into its contributions along the local x (left) and y-directions (right). The statistical error visualised by the error bars was computed based on block averages using 20 blocks.

along the heptagon axis rather than enhancing the existing tilt along the pentagons. Finally, divacancies show a slightly higher gradient along the pentagon axis relative to the octagon axis. This observation is persistent throughout the entire concentration range investigated in this work.

12 Comparison to established force fields

To compare our findings obtained with the GAP-20 [1] with the predictions based on established force fields, we conducted additional MD simulations with two commonly used interatomic potentials, namely the long-range carbon order potential (LCBOP) [18] and the reactive empirical bond order (REBO II) potential [19]. In particular, we are interested in the predicted morphology profiles and the related corrugation of the graphene sheet in the abundance of defects. Therefore, we focus our comparison on the CAF at a defect concentration of 1%. For both defect types, we initialise the simulations from the same defect distribution as one of our GAP-based simulations reported in the manuscript. To achieve a fair comparison, the same production lengths were employed as reported in the manuscript, i.e. 150 ps and 1 ns for defective and pristine graphene, respectively.

The results of this comparison are summarised in figure S11. While the CAF predicted for system comprising Stone-Wales defects agree well between the different force fields, large deviations are observed in the presence of divacancies. In contrast to the GAP-driven simulations, we do not find a significant corrugation enhancement and the systems morphology resembles that one of pristine graphene. The origin of this deviation lies in the natural reconstruction of the divacancy defect into two 5-membered and an 8-membered ring as observed in the GAP-based trajectories which is not predicted by both established models. Consequently, the divacancy defects merely behave like holes in the surface and

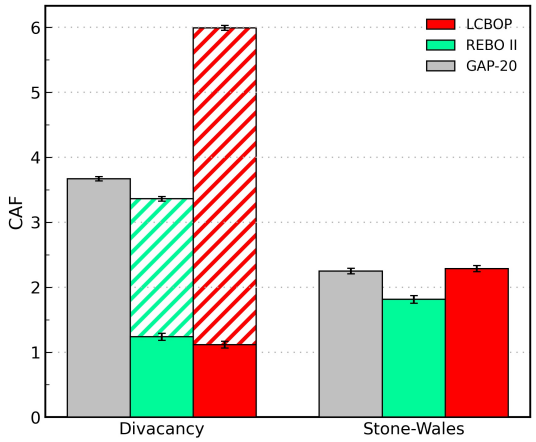

Figure S11: Comparison of the CAF for both defect types at 1 % defect concentration for different interatomic potentials. The hatched bars for the simulations based on REBO II and LCBOP were initialised with reconstructed divacancies. The statistical error visualised by the error bars was computed based on block averages using 20 blocks.

cannot induce corrugation in the way described by the GAP-20. This is presumably caused by the potentials' short cutoffs, 2 Å and 2.2 Å for REBO II and the short-range part of LCBOP, leading to an overestimated energy barrier associated with the reconstruction. Indeed, starting the simulation from a sheet comprising divacancy defects in their reconstructed configuration (hatched bars in figure S11) results in morphology profiles which can be even more corrugated than predicted by the GAP-20.

References

[1] P. Rowe, V. L. Deringer, P. Gasparotto, G. Csányi, and A. Michaelides, "An accurate and transferable machine learning potential for carbon," *Journal of Chemical Physics*, vol. 153, p. 034702, 2020.

[2] S. Plimpton, "Fast Parallel Algorithms for Short-Range Molecular Dynamics," *Journal of Computational Physics*, vol. 117, no. 6, pp. 1–19, 1995.

[3] A. Hjorth Larsen, J. JØrgen Mortensen, J. Blomqvist, I. E. Castelli, R. Christensen, M. Dułak, J. Friis, M. N. Groves, B. Hammer, C. Hargus, E. D. Hermes, P. C. Jennings, P. Bjerre Jensen, J. Kermode, J. R. Kitchin, E. Leonhard Kolsbjerg, J. Kubal, K. Kaasbjerg, S. Lysgaard, J. Bergmann Maronsson, T. Maxson, T. Olsen, L. Pastewka, A. Peterson, C. Rostgaard, J. SchiØtz, O. Schütt, M. Strange, K. S. Thygesen, T. Vegge, L. Vilhelmsen, M. Walter, Z. Zeng, and K. W. Jacobsen, "The atomic simulation environment - A Python library for working with atoms," *Journal of Physics Condensed Matter*, vol. 29, p. 273002, 2017.

[4] N. Michaud-Agrawal, E. J. Denning, T. B. Woolf, and O. Beckstein, "Software News and Updates MDAnalysis: A Toolkit for the Analysis of Molecular Dynamics Simulations," *Journal of computational chemistry*, vol. 32, pp. 2319–2327, 2011.

[5] R. Gowers, M. Linke, J. Barnoud, T. Reddy, M. Melo, S. Seyler, J. Domański, D. Dotson, S. Buchoux, I. Kenney, and O. Beckstein, "MDAnalysis: A Python Package for the Rapid Analysis of Molecular Dynamics Simulations," *Proceedings of the 15th Python in Science Conference*, pp. 98–105, 2016.

[6] A. Stukowski, "Visualization and analysis of atomistic simulation data with

OVITO-the Open Visualization Tool," *Modelling and Simulation in Materials Science and Engineering*, vol. 18, p. 015012, 2010.

[7] F. L. Thiemann, P. Rowe, E. A. Müller, and A. Michaelides, "Machine Learning Potential for Hexagonal Boron Nitride Applied to Thermally and Mechanically Induced Rippling," *The Journal of Physical Chemistry C*, vol. 124, pp. 22278–22290, 2020.

[8] D. R. Nelson and L. Peliti, "Fluctuations in Membranes With Crystalline and Hexatic Order.," *Journal de physique Paris*, vol. 48, no. 7, pp. 1085–1092, 1987.

[9] P. Le Doussal and L. Radzihovsky, "Self-consistent theory of polymerized membranes," *Physical Review Letters*, vol. 69, no. 8, pp. 1209–1212, 1992.

[10] D. R. Nelson, T. Piran, and S. Weinberg, eds., *Statistical Mechanics of Membranes and Surfaces*. Singapore: World Scientific, 2 ed., 2004.

[11] C. G. Wang, L. Lan, Y. P. Liu, and H. F. Tan, "Defect-guided wrinkling in graphene," *Computational Materials Science*, vol. 77, pp. 250–253, 2013.

[12] L. He, S. Guo, J. Lei, Z. Sha, and Z. Liu, "The effect of Stone-Thrower-Wales defects on mechanical properties of graphene sheets - A molecular dynamics study," *Carbon*, vol. 75, no. Md, pp. 124–132, 2014.

[13] O. Lehtinen, S. Kurasch, A. V. Krasheninnikov, and U. Kaiser, "Atomic scale study of the life cycle of a dislocation in graphene from birth to annihilation," *Nature Communications*, vol. 4, p. 2098, 2013.

[14] J. Kotakoski, A. V. Krasheninnikov, U. Kaiser, and J. C. Meyer, "From point defects in graphene to two-dimensional amorphous carbon," *Physical Review Letters*, vol. 106, p. 105505, 2011.

[15] W. Bao, F. Miao, Z. Chen, H. Zhang, W. Jang, C. Dames, and C. N. Lau, "Controlled ripple texturing of suspended graphene and ultrathin graphite membranes," *Nature Nanotechnology*, vol. 4, no. 9, pp. 562–566, 2009.

[16] P. Rowe, G. Csányi, D. Alfè, and A. Michaelides, "Development of a machine learning potential for graphene," *Physical Review B*, vol. 97, p. 054303, 2018.

[17] J. Ma, D. Alfè, A. Michaelides, and E. Wang, "Stone-Wales defects in graphene and other planar s p2 -bonded materials," *Physical Review B - Condensed Matter and Materials Physics*, vol. 80, p. 033407, 2009.

[18] H. Los and A. Fasolino, "Intrinsic long-range bond-order potential for carbon: Performance in Monte Carlo simulations of graphitization," *Physical Review B - Condensed Matter and Materials Physics*, vol. 68, p. 024107, 2003.

[19] S. J. Stuart, A. B. Tutein, and J. A. Harrison, "A reactive potential for hydrocarbons with intermolecular interactions," *Journal of Chemical Physics*, vol. 112, no. 14, pp. 6472–6486, 2000.